Geophysical Journal International

Geophys. J. Int. (2022) **230,** 317–333
Advance Access publication 2022 February 24
GJI Seismology

https://doi.org/10.1093/gji/ggac080

Joint inversion of receiver functions and surface wave dispersion in the Recôncavo–Tucano basin of NE Brazil: implications for basin formation

M.F. Döring,[1] J. Julià [1,2] and M. Evain [3]

[1] *Programa de Pós-Graduação em Geodinâmica e Geofísica - UFRN, Natal, RN CEP* 59078-970. *E-mail: jordijc@gmail.com*
[2] *Departamento de Geofísica–UFRN, Natal, RN CEP* 59078-970
[3] *IFREMER, Marine Geosciences, Centre de Brest, CS10070,* 29280 *Plouzane, France*

Accepted 2022 February 22. Received 2022 February 15; in original form 2021 July 13

SUMMARY

The crustal structure of the Recôncavo–Tucano basin, an aborted rift system that developed in NE Brazil during extension related to the opening of the South Atlantic Ocean, has been investigated through local constraints from receiver functions developed at 18 seismic stations in the region. Gravity modelling has proved unable to unequivocally localize crustal thinning under the basin depocentre and, together with a general lack of sediments from a putative thermal sag phase, this has led to a range of basin formation models invoking either pure or simple shear or a combination of both. In particular, the 'flexural cantilever' model has assumed simple shear extension in the upper crust and pure shear extension in the lower crust and mantle, enabling local erosion of the rift flanks after footwall uplift and regional erosion of the thermal sag phase after magmatic underplate of the basin's crust. Our results reveal that the crust is over 40 km thick beneath the Tucano and Recôncavo basins and that it contains a thick (5–8 km) layer of high velocity ($Vs > 4.0$ km s^{-1}) material below ∼35 km depth. These observations contrast with structure immediately West (São Francisco Craton) and East (Borborema Province) of the basin, for which crustal thicknesses average 42 and 36 km, respectively, lower crustal velocities are below 4.0 km s^{-1}, and local instances of crust as thin as 33.5 km are observed. We propose, in agreement with the 'flexural cantilever' model, that the fast velocity layer making the basin's lowermost crust resulted from mafic underplating after stretching and thinning during the syn-rift phase, restoring crustal thickness to pre-rift values (or larger) and providing the necessary buoyancy to trigger regional uplift. Moreover, although not pervasive, instances of thin crust along the footwall could be related to rift flank erosion. We thus conclude that, regardless of the mode of extension in the upper crust, our results favour models of basin formation invoking extension of the lower crust by pure shear.

Key words: South America; Joint Inversion; Crustal imaging; Continental tectonics: extensional.

1 INTRODUCTION

Two main paradigms have been traditionally accepted when considering extensional tectonics and the formation and evolution of rift basins. The lithospheric stretching model of McKenzie (1978) proposes that uniform extension of the lithosphere leads to rapid mechanical subsidence (syn-rift) of the crust, which is then followed by slower thermal subsidence (post-rift) driven by the cooling of mantle advected during the syn-rift stage. The model invokes pure shear as the main style of deformation, and predicts that crustal thinning should develop immediately below the sedimentary basin. In contrast, the simple shear model of Wernicke (1985) invokes accommodation of extension through large-scale detachment zones crossing the crust and lithospheric mantle, with formation of a rift basin in the upper portion of the detachment and thinning of the crust and lithosphere downdip along the detachment fault. The main predictions of this model are the lack of thermal subsidence in the rift basin and the offset of crustal thinning away from the basin depocentre. Both models are valid solutions for extensional tectonics and have been invoked to explain the formation and evolution of rift basins worldwide (see e.g. Cloetingh & Burov 2011).

In NE Brazil, extensional stresses related to the opening of the South Atlantic Ocean in Mesozoic times resulted in a network of rift basins that aligned along three main axis of deformation (Matos 1992, 1999): Recôncavo–Tucano–Jatobá (RTJ), Gabon–Sergipe–Alagoas (GSA) and Cariri–Potiguar (CP). Continental breakup

eventually succeeded along the GSA trend and aborted along the RTJ and CP trends, leaving in the way a number of marginal basins off-shore and aborted rift basins on-shore. How extensional stresses affected its crust and lithospheric mantle, however, is still debated, as both pure and simple shear models have been invoked to explain middle and lower crustal deformation as well as mantle deformation (Ussami *et al.* 1986; Milani & Davison 1988; Magnavita *et al.* 1994; Blaich *et al.* 2008). The system of syn-rift basins that resulted from extension in NE Brazil represents a unique window into the evolution of passive continental margins in general; it is thus critical to fully integrate their crustal architecture, depositional and tectonic histories if we are to understand the role that extensional stresses play in the formation and evolution of rift basins.

More in particular, a number of disparate competing models have been proposed for the formation and evolution of the Recôncavo–Tucano basin (Fig. 1). This on-shore basin system shares pre- and syn-rift depositional histories with the marginal Sergipe–Alagoas and Jacuipe basins, but differs in the lack a thick post-rift depositional sequence (e.g. Ussami *et al.* 1986; Mohriak *et al.* 2000). Taking this into account, Ussami *et al.* (1986) proposed that a single lithospheric-scale detachment could have been responsible for accommodating synchronous syn-rift extension along the Tucano and Jacuípe sub-basins, with thermal subsidence developing only on the latter. Castro Jr (1987) additionally recognized the change in polarity of the main bounding faults along the full Recôncavo–Tucano system, and devised a system of coupled double detachments to explain the synchronous syn-rift evolution of the Recôncavo–Tucano basin system and their related marginal basins. Davison *et al*. (1988) and Milani & Davison (1988) on the other hand, challenged the feasibility of the proposed simple shear models and advocated for pure shear extension in the lower and middle crust for this basin system, with independent evolution for the interior and marginal rift basins. At the heart of this debate was the ambiguity of gravity modelling in constraining crustal thinning. Simple shear models relied on gravimetric profiles that showed thinner crust laterally offset with respect to the basins depocentres (Ussami *et al.* 1986 Castro Jr 1987), while pure shear models were based on similar gravimetric profiles that instead showed crustal thinning right under the basins (Milani & Davison 1988).

Later evolutionary models for the Recôncavo–Tucano basin did not settle the controversy. Magnavita *et al.* (1994) used the erosional and exhumation history of the RTJ basins and surrounding areas to constrain the 'flexural cantilever' model of (Kusznir & Ziegler 1992), in which simple shear in the upper crust and pure shear in the lower crust and lithospheric mantle are capable of explaining basin architecture without need of lithospheric-scale detachments. Moreover, although no modelling of the deep crust was involved, post-rift magmatic underplating was invoked in order to explain a major break in the stratigraphic record. Mohriak *et al.* (2000), through integration of gravity surveys and deep seismic reflection profiles, concluded that rifting started with regional lithospheric extension over a wide region, forming rifts along pre-existing zones of crustal weakness to subsequently focus on deeper mantle weak zones. Although not explicitly stated, the narrative suggests simple shear would be the main style of deformation. Finally, Blaich *et al.* (2008) made a comprehensive attempt at gravity modelling along the NE Brazil margin, aided by regional deep vertical-incidence and wide angle seismic data, to find distinct structural and magmatic changes along the margin, and proposed a polyphase evolution in which deformation would initiate as pure shear to then continue as simple shear.

In this paper, we attempt to discriminate among the various competing models by developing new constraints on crustal thickness and velocity structure from analysis of *P*-to-*S* conversions in teleseismic receiver functions. Receiver functions have become a standard technique for investigating crustal structure (e.g. Rondenay *et al.* 2017) and have been successfully applied in a number of tectonic settings including sedimentary basins (e.g. Coelho *et al.* 2018; Cedraz *et al.* 2020; Nemocon *et al.* 2021). Teleseismic waveforms were recorded by a network of 21 seismic stations deployed in and around the Recôncavo, Tucano and Sergipe-Alagoas basins, which included 15 broad-band stations and 6 short-period stations. These data were used to develop receiver function estimates and, through waveform modelling (Julia *et al.* 2003) and H–κ stacking (Zhu & Kanamori 2000), produce estimates of crustal thickness, bulk Vp/Vs ratio and depth-dependent *S*-wave velocity for all the stations making up the network. Our results show that crustal thicknesses under the Tucano and Recôncavo basins are similar to those found in adjacent areas outside the basins, mostly due to the presence of a thick (5–8 km), fast-velocity (>4.0 km s^{-1}) lowermost crust. Perhaps more puzzlingly, our results also reveal crustal thinning immediately east of the Central Tucano basin. We argue, in agreement with the 'flexural cantilever' model of Magnavita *et al.* (1994), that the high-velocity lowermost crust resulted from mafic intrusions and that crustal thinning could be the result of rift-flank erosion, thus favouring pure shear deformation of the middle/lower crust and lithospheric mantle under NE Brazil during Mesozoic extension.

2 GEOLOGY AND TECTONIC SETTING

Following Milani & Davison (1988), the RTJ rift can be regarded as a series of asymmetric half-grabens that are separated by basement highs and transfer faults (Fig. 1). The axis of the system trends in a general N–S direction, but a number of well-defined transfer faults that cross the rift system show that the opening took place in a more oblique NW direction. The transfer faults naturally divide the rift into four sub-basins: Recôncavo, South and Central Tucano, North Tucano and Jatobá, with the main rift faults dipping eastward in the Northern Tucano and westward in the Recôncavo and South Tucano. The flipping of the half-graben asymmetry occurs across the Vaza-Barris Transfer Zone (VBTZ), thus offsetting the basin depocentres to the western side of Northern Tucano and to the eastern side of South Tucano and Recôncavo. The VBTZ also marks the southernmost termination of the Sergipe–Alagoas basin and the northernmost termination of the Jacuipe–Gabon basin (Castro Jr 1987), preserving the asymmetry of the half-grabens and the offsetting of the basins depocentres.

2.1 Stratigraphy, exhumation and erosion

The opening of the RTJ rift started during early Cretaceous times, but virtually all rift-related sedimentation occurred in the Mesozoic (Magnavita *et al.* 1994). Thus, although older sedimentary cycles might still be outcropping due to erosion of the Mesozoic rocks, Mesozoic sedimentation closely follows the tectonic evolution of the basin and is arranged according to pre-rift, syn-rift and post-rift sequences (Fig. 2).

The pre-rift stage spanned from the Late Jurassic to the Early Cretaceous, and includes continental sandstones and lacustrine shales making the Dom João and lower Rio da Serra formations, with

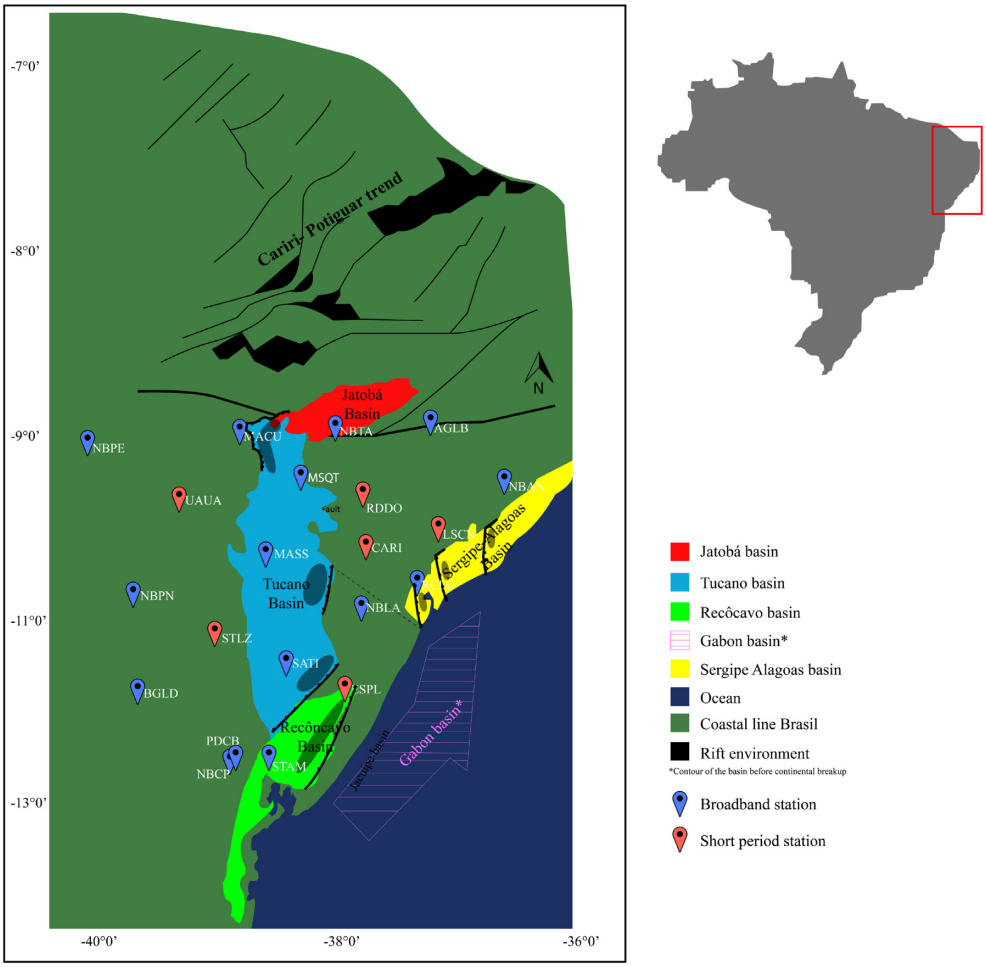

Figure 1. Map of all broad-band (blue) and short-period (red) stations utilized in this study, with the Jatobá (red), Tucano (blue), Recôncavo (green) and Sergipe-Alagoas (yellow) basin outlined. Transparent grey shadows are depocentre locations for all of the basins and black lines represent main master and transfer faults (modified from Castro Jr 1987).

thicknesses that range from 200 m (Jatobá) to 1200 m (Recôncavo). The syn-rift stage occurred during the Berriasian (∼140 Ma) and lasted for 24 Ma. Stratigraphically, this period includes the sequences from the Rio da Serra to the Jiquiá formations. Sedimentary strata deposited during this period consisted mostly of up to 3 km of non-marine sandstones and shales, which can be found both on the African and South American margins. The end of the rifting phase occurred during Aptian times, and was followed by a post-rift phase with predominantly slow rates of subsidence. Post-rift sedimentation is small-volume (up to 400 m), and consists mostly of the lacustrine shale deposits belonging to the Marizal formation. There is an apparent unconformity between the Cretaceous sediments and the deposits of the Aptian Marizal formation throughout the entire RTJ rift (Silva 1993), which Magnavita *et al.* (1994) related to an erosion event at 124–120 Myr. The depositional history of the RTJ basin ends in the Miocene with deposition of the Sabiá and Barreiras formations in the Recôncavo sub-basin and deposition of Quaternary sediments in all the sub-basins. These sediments were deposited unconformably on top of the older Marizal formation, suggesting a second period of uplift and erosion prior to Miocene times (Magnavita *et al.* 1994).

Notably, the RTJ rift basins seem to be devoid of any syn- or post-rift magmatic activity (Magnavita *et al.* 1994; Mohriak *et al.* 2000). The closest intrusions consist of three subparallel dolerite dykes East of the Tucano basin, with K-Ar dates of 105 ± 9 Ma, which were inferred indirectly from aeromagnetic and outcrop data (Magnavita *et al.* 1994). Rift-related magmatism seems to be restricted to break-up along the associated marginal basins, where it has been identified as either fast-velocity (>7.0 km s^{-1}) lowermost crustal bodies in refraction lines or small-volume, on-shore mafic intrusives (Blaich *et al.* 2008; Pinheiro *et al.* 2018).

Deposition along the RTJ basins parallels deposition in the marginal Sergipe–Alagoas and Jacuipe basins of Brazil and the Gabon basin of West Africa, except for the 2–3 km of sedimentary rocks associated with the thermal subsidence phase (Chang *et al.* 1988; Teisserenc & Villemin 1989; Matos 1992, 1999). The absence of a full stratigraphic record of the thermal stage in the RTJ basins is noteworthy, as it has been invoked to support crustal-scale detachments (Ussami *et al.* 1986; Castro Jr 1987) in the region and simple shear extension as the main style of deformation. Prolonged mechanical stretching of the lithosphere during the rift phase (Milani & Davison 1988) or removal of post-rift sediments after uplift and erosion of the RTJ rift (Magnavita *et al.* 1994), however, have been proposed as alternative mechanisms compatible with pure shear extension as the main mode of deformation.

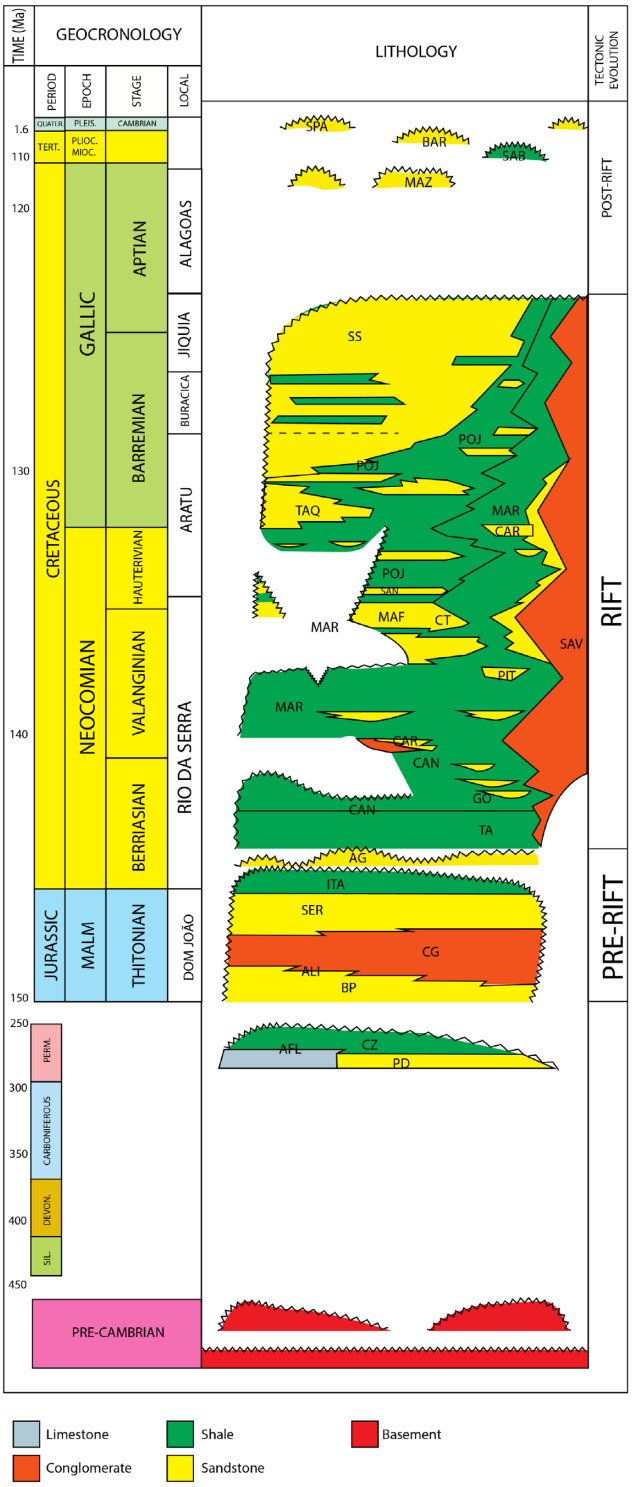

Figure 2. Stratigraphic chart of the Recôncavo–Tucano basin, classified as Recôncavo Series. Modified from Viana *et al.* (1971). BP, Boipeba; CG, Capianga; SER, Sergi; AG, Água Grande; CAN, candeias; TA, Tauá; GO, Gomo; MAR, Maracangalha; CAR, Caruaçu; PIT, Pitanga; MAF, Marfim; CT, Catu; POJ, Pojuca; SAV, Salvador; SS, Sesmaria; MAZ, Marizal; SAB, Sabiá; BAR, Barreiras. Adapted from (Caixeta *et al.* 1994).

2.2 Extensional models

There is a long-standing debate about the nature of the processes that culminated in the formation of the on-shore basins of NE Brazil, especially in regard to the rheological behaviour of the lithosphere under extensional stresses (Ussami *et al.* 1986; Castro Jr 1987; Milani & Davison 1988; Magnavita *et al.* 1994; Mohriak *et al.* 2000; Blaich *et al.* 2008). In particular there is an active debate about extension being accommodated through pure shear, simple shear, or both. As a result, a number of models have been proposed to explain the formation of the RTJ rift and adjacent marginal basins.

Ussami *et al.* (1986) invoked a single, east verging low-angle detachment surface to explain the linked development of the on-shore and off-shore basins along the Brazilian continental margin between 8° and 14°S (Fig. 3c). The detachment surface was postulated after a crustal cross-section crossing the Central Tucano and Jacuipe basins. The cross-section was constrained by gravity data and displayed a uniform 30-km-thick crust along the entire on-shore portion of the profile that rapidly thinned down to 10 km under the off-shore portion. Accommodation of extension through simple shear would have developed simultaneously in the upper crust for both the on-shore and off-shore basins, with the collapse of the hanging wall forming the on-shore basins and the upwarp of the footwall enabling concentration of deep lithospheric extension under the off-shore basins and thermal subsidence. Castro Jr (1987) added gravimetric data in the São Francisco craton and expanded the crustal cross-section of Ussami *et al.* (1986) to the West. The expanded cross-section revealed a 35-km-thick crust under the craton and a locally thin crust of about 20 km immediately West of the Tucano basin. He proposed a double west verging detachment system in which the South Tucano–Recôncavo and Jacuipe–Gabon basins would have formed after the collapse of the corresponding hanging walls (Fig. 3d). Moreover, he acknowledged that the half-grabens making the RTJ basins change polarity across the Vaza-Barris transfer fault, and postulated that a similar east verging, double detachment system could be responsible for the formation of the North Tucano and Sergipe–Alagoas basins.

The plausibility of crustal-scale detachment surfaces linking the on-shore Tucano basin and associated off-shore basins was challenged by Davison *et al.* (1988). The author first noticed that the residual maximum negative anomalies along the gravity profile of Castro Jr (1987) closely coincided with the maximum depocentre revealed by reflection and refraction profiling, which would be suggestive of important crustal thinning below the Tucano basin and not away from it. Indeed, gravity modelling along several profiles crossing the Recôncavo and Tucano basins presented in Milani & Davison (1988) displayed a 35 km thick crust over the region with localized crustal thinning of 20–25 km under the basins depocentres. The author also noticed that Precambrian mobile belt structures (shear zones, faults, fold axial planes), which would constitute likely candidates for the development of reactivated detachment zones, were steeply dipping and not trending parallel to the basin master faults. He further argued that, as stretching factors were similar for the upper and the whole crust and the prolonged time span (20–30 Myr) over which crustal extension occurred would equally explain the lack of thermal subsidence, pure shear extension for the middle and lower crust was more likely. Moreover, as the Sergipe–Alagoas basin displays more complex deformation, he further argued that

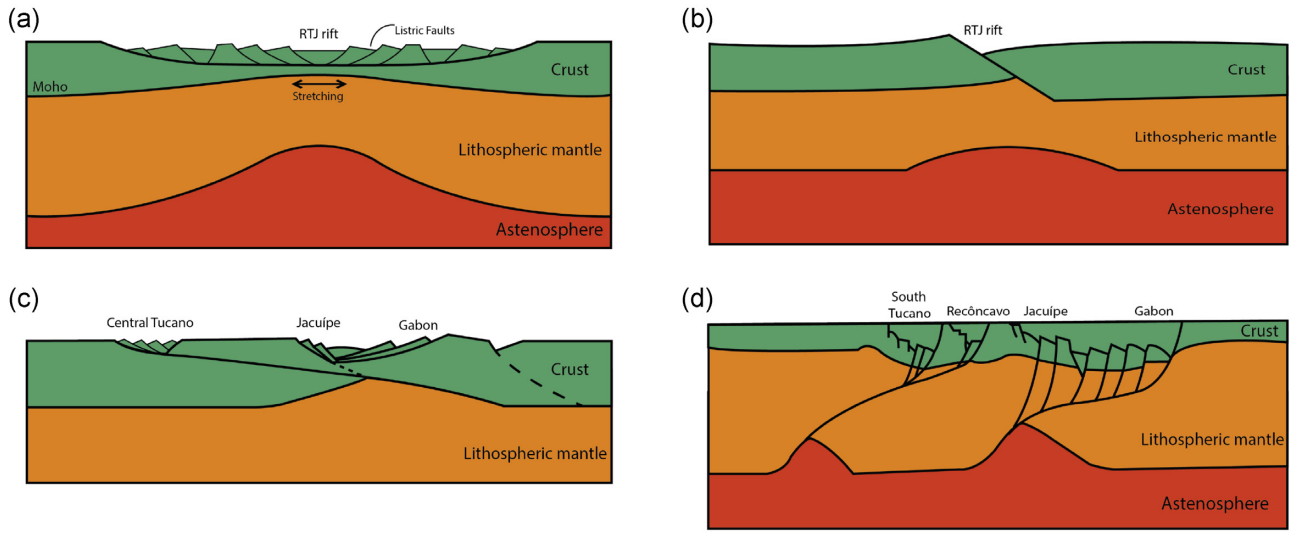

Figure 3. Examples of current extension models for the Recôncavo–Tucano rift and adjacent basins (a) Pure shear extension model invoked by Milani & Davison (1988), as originally proposed by McKenzie (1978); (b) Cantilever model proposed by Kusznir & Ziegler (1992); (c) Simple shear (single detachment) extension model of Ussami *et al.* (1986) and (d)Simple shear (double detachment) extension model of Castro Jr (1987).

on-shore and off-shore basins would have had separate tectonic developments.

In spite of the plausibility of the models above, none of them took into account the exhumation and erosion histories of the rift basins. Recall that two periods of uplift and erosion were identified in the stratigraphic record (Magnavita *et al.* 1994): one at 124–120 Myr, accounting for the unconformity between the Cretaceous sediments and the Aptian Marizal formation, and another one of unknown age but preceding deposition of the Pliocene Barreiras Formation. Magnavita *et al.* (1994) incorporated those histories into the flexural cantilever model of Kusznir & Ziegler (1992) by matching basement depths along several seismic cross-sections traversing the RTJ basin system. The cantilever model combines simple shear for the brittle upper crust and pure shear for the lower crust and uppermost mantle (Fig. 3b), so that variations in crustal thickness and temperature in the lithosphere are compensated through flexural isostasy. More importantly, extension along planar faults in the upper crust is isostatically accommodated through collapse of the hanging wall and uplift of the footwall, thus behaving as two mutual self-supporting flexural cantilevers. The flexural cantilever model naturally explains the Aptian unconformity through large footwall uplift and up to 5 km of subsequent erosion along the basin-bounding faults. Erosion of the post-rift sediments, on the other hand, requires an *a priori* regional uplift of 200–600 m that the authors attribute to an unknown, late magmatic underplating event. The authors further note that, assuming Airy isostasy, 600 m of uplift would require about 3.5 km of underplated magma representing about 400 000 km^3 of magma intrusion in the crust.

Mohriak *et al.* (2000) returned to the simple extension models after compiling deep seismic reflection and gravity data to construct a crustal transect crossing the Central Tucano and Sergipe–Alagoas basin. The combined geotransect displayed a 30–32-km-thick crust along the profile that locally thins to 26–28 km immediately East of the Tucano basin and to about 12 km under the off-shore Sergipe–Alagoas basin, much in agreement with the gravimetric interpretation of Ussami *et al.* (1986). They argue that the two zones of crustal necking suggest extension was first distributed over a wide region, perhaps along pre-existing weakness zones in the crust, to subsequently focus along a deeper mantle weak zone that eventually resulted in rupture of the plate.

Finally, Blaich *et al.* (2008) performed extensive gravity modelling for several transects along the entire NE Brazil margin that revealed distinct along-margin structural and magmatic changes, suggestive of margin segmentation and evolution across transfer systems. Gravity modelling was constrained by available seismic data when possible, and displayed average crustal thicknesses of 30–36 km with local thinning of 26–30 km under the Central Tucano and Recôncavo basins and 15–20 km under the off-shore Jacuipe and Sergipe–Alagoas basins. Most interestingly, the models included a layer of high-density mafic material under the off-shore basins that was identified in seismic reflection profiles. Along with results from a similarly constructed transect along the conjugate African margin, they advocated for polyphasic rifting to explain the extensional history of the passive margins. They argued that initial pure shear extension characterized by the formation of listric faults near the surface and crustal thinning below the basins, would have been followed by simple shear extension, during which the listric faults would have been overprinted by westward dipping local detachments. Moreover, their modelling provided evidence that the margins, at least in part, would have evolved with volcanic activity.

3 DATA, RECEIVER FUNCTIONS AND DISPERSION

3.1 Seismic deployments

Data for this study was acquired as part of a broader project that focuses on investigating the sedimentary architecture of the syn-rift basins of NE Brazil with passive-source seismology. The project, funded by the national oil company Petrobras, deployed a total of 20 seismic stations in and around those basins for a period of around 2 yr. Up to 11 stations were installed along the RTJ rift and included: 6 broad-band stations equipped with Nanometrics Meridian Compact post-hole seismometers, with flat velocity response between 120 s and 108 Hz and integrated high-gain digitizers; and 5 short-period stations equipped with Sercel L4A-3D seismometers with

flat velocity response above 2 Hz feeding Reftek-130 high-gain digitizers. The broad-band stations belonged to the *Laboratório Sismológico* of the *Universidade Federal do Rio Grande do Norte* (LabSis/UFRN), while the short-period stations were taken from the *Pool de Equipamentos Geofísicos do Brasil* (PEGBR). All stations used GPS antennas for timekeeping and operated continuously with sampling rates of 100 samples per second (sps).

These stations complemented 6 permanent broad-band stations belonging to the *Rede Sismográfica do Nordeste* (RSisNE), which is part of the Rede Sismográfica Brasileira (RSBR), and are equipped with RefTek 151-120 sensors and RefTek-130 digitizers (24-bit) sampling at 100 Hz (Bianchi *et al.* 2018); 2 broad-band stations from the temporary Brazilian Lithospheric Seismic Project (BLSP), equipped with STS-2 Streckeisen sensors and 24-bit RT-130 digitizers also sampling at 100 Hz (Assumpção *et al.* 2004) and 2 seismic stations (1 broad-band and 1 short-period, with same specifications as the project stations) deployed by the LabSis/UFRN to monitor local seismic activity near Baixa Grande, BA and Canhoba, SE, respectively.

Overall, the combined network for this study consisted of 21 seismic stations (15 broad-band and 6 short-period) covering the RTJ rift and surrounding areas (Fig. 1). Station locations, sensor types and recording periods are summarized in Table 1.

3.2 Receiver functions

Receiver functions are time-series obtained through deconvolution of the vertical component of teleseismic *P*-wave recordings from the corresponding radial component (Langston 1979). The deconvolution operation isolates the structural response below a given seismic station from instrument and source effects, effectively equalizing the resulting time series. The peaks and troughs making up receiver functions represent *P*-to-*S* conversions formed after the interaction of an incoming teleseismic *P*-wavefront with subsurface discontinuities local to the recording station. The most prominent conversions are developed through refraction at the Moho (*Ps*) and multiple reverberations between the Moho and the free surface (PpPms, PpSms+PsPms). Thus, modelling of the amplitudes and *S*–*P* arrival times of each conversion allows to constrain variations of *S*-velocity with depth under the seismic station (e.g. Ammon *et al.* 1990; Owens & Taylor 1984).

All teleseismic *P* waves included in this study were selected from events with magnitude above 5.0 m_b and epicentral distances between 30° and 90°. The corresponding waveforms were windowed 10 s before and 110 s after the arrival of the direct *P* wave, demeaned, detrended and tapered, and high-pass filtered above 0.05 Hz to reduce low-frequency instrumental noise. An anti-alias low-pass filter below 4 Hz was applied to the seismic waveforms before decimation to 10 sps. Before deconvolution, the seismograms were rotated into the great-circle-path to obtain the radial and transverse seismogram components.

To reduce numeric instability associated with signal-generated noise (Langston & Hammer 2001), we used the iterative, time-domain deconvolution of Ligorría & Ammon (1999) to compute the receiver functions. This is a least-squares based method that calculates the receiver function after minimizing the difference between the horizontal (radial or transverse) seismogram and the corresponding vertical seismogram convolved with a spike train (the receiver function). The spike train is iteratively updated by adding a spike that reduces the mismatch after each iteration. Receiver functions were produced at two overlapping frequency bands, after filtering the deconvolved spike train with Gaussian filter widths of 1.0 ($f < 0.5$ Hz) and 2.5 ($f < 1.2$ Hz). Receiver function amplitudes are frequency-dependent when gradational boundaries are present (see e.g. Julià 2007), so overlapping frequency contents help discriminate against sharp subsurface discontinuities.

Quality control consisted of removing all receiver functions that did not reproduce at least 85 per cent of the original radial seismogram when convolved back with the corresponding vertical seismogram. This step eliminated, on average, 80 per cent of the receiver functions originally computed. Additionally, receiver functions waveforms with either patterns significantly different from the average or with anomalously large transverse amplitudes were visually removed. This second step eliminated, on average, an additional 50 per cent of the receiver function data set. The final number of selected receiver functions at each seismic station is given in Table 1. The large variability in selected receiver functions reflects both the large variability in recording times between permanent and temporary stations and instrument malfunctions in some temporary stations.

As an illustration, Fig. 4 shows radial and transverse receiver functions (Gaussian width of 2.5 and 1.0) at two select stations in the Tucano sub-basin (MASS) and the São Francisco craton (STLZ). Note that MASS corresponds to a broad-band site while STLZ corresponds to a short-period site (Table 1). Receiver functions were binned by backazimuth and ray parameter and averaged within each bin, with maximum variations of 10° and 0.01 s km^{-1}, respectively. Binning by ray parameter is required before averaging to avoid cancellation of receiver function amplitudes due to phase moveout, while binning by backazimuth is useful to assess lateral heterogeneity around the station. Ps conversions at the Moho are quite apparent at around 5 s for most receiver functions, in spite of station MASS being located on top of sedimentary rocks. Sedimentary structure can disrupt deeper conversions significantly (Julia` *et al.* 2004; Zelt & Ellis 1999) but, in this case, it seems its signature is restricted to the first 3–4 s and does not interfere significantly with deeper *P*-to-*S* conversions. Also, transverse receiver functions for station MASS display some sizeable amounts of energy for all backazimuths, likely due to complex basement geometry; a good azimuthal coverage is therefore important so that average 1-D structure is recovered from joint receiver function modelling. At the short-period station STLZ, on the other hand, transverse amplitudes are generally smaller than the corresponding radial amplitudes and suggest that variations of seismic velocity with depth is predominant. Finally, note that receiver functions were obtained with similar overlapping frequency contents in spite of the original waveforms being recorded in different bands. This is because the deconvolution process effectively extends the velocity response beyond its original flat portion (Julià *et al.* 1998; Ligorría & Ammon 1999).

3.3 Dispersion velocities

Dispersion curves were taken from the continent-wide surface-wave tomography study of Feng *et al.* (2004). In that study, group velocity was measured on regional waveforms through application of a Multiple Filtering Technique (MFT, Dziewonski *et al.* 1969) with phase-matching (Herrin & Goforth 1977) to isolate the fundamental mode surface-wave. The tomography was performed on a grid of 2° × 2° cells, where group velocity was determined for each cell by minimizing the root mean square between observations and predictions through the conjugate-gradient method (Paige & Saunders 1982) with *a priori* smoothness constraints for each period. Thus,

Table 1. Station names, locations, sensor types, recording period described as Julian day/year and number of receiver functions for each Gaussian width.

Station code	Lat. (°)	Lon. (°)	Sensor type	Recording period day/year	# of rec. fun. (a = 2.5)	# of rec. fun. (a = 1.0)
AGBL	−9.03	−37.04	BB	133/2010–133/2011	13	16
BGLD	−11.84	−40.16	BB	092/2018–181/2018	1	1
CARI	−10.36	−37.73	SP	296/2018–106/2019	2	2
ESPL	−11.83	−37.95	SP	099/2019–287/2019	11	8
LSCN	−10.17	−36.97	SP	185/2019–287/2019	4	6
MACU	−9.15	−39.05	BB	146/2019–308/2020	19	14
MASS	−10.43	−38.78	BB	280/2018–308/2020	26	33
MSQT	−9.64	−38.41	BB	146/2019–308/2020	26	30
NBAN	−9.66	−36.27	BB	245/2011–338/2018	57	66
NBCP	−12.58	−39.18	BB	271/2011–051/2013	21	15
NBLA	−10.99	−37.78	BB	248/2011–356/2018	99	108
NBPE	−9.24	−40.68	BB	136/2013–362/2013	9	12
NBPN	−10.84	−40.19	BB	271/2011–356/2018	126	108
NBTA	−9.12	−38.06	BB	209/2011–246/2018	114	98
PDCB	−12.53	−39.12	BB	267/2002–062/2004	15	14
RCLO	−10.73	−37.19	BB	146/2019–287/2019	22	19
RDDO	−9.80	−37.77	SP	146/2019–194/2019	15	10
SATI	−11.55	−38.58	BB	146/2019–208/2020	5	9
STAM	−12.55	−38.77	BB	280/2018–308/2020	30	33
STLZ	−11.24	−39.33	SP	269/2018–108/2019	11	9
UAUA	−9.84	−39.70	SP	146/2019–287/2019	9	4

a total of 12 000 paths were analysed resulting in 6500 Rayleigh-wave and 3500 Love-wave dispersion curves for periods between 10 and 150 s for Rayleigh waves and 20–70 s for Love waves. For the joint inversion methodology utilized here, only Rayleigh-wave dispersion was considered.

4 RESULTS

4.1 Joint inversion

In order to investigate crustal structure beneath the Recôncavo–Tucano sub-basins, *S*-wave velocity–depth profiles for each station were developed by inverting receiver function waveforms jointly with dispersion curves. The combination bridges resolution gaps between the data sets, and produces velocity–depth profiles with a minimal degree of non-uniqueness and little dependence on the starting model. The approach, developed by Julia *et al.* (2000; 2003), minimizes the root mean square (RMS) misfit between observations and predictions in an iterative fashion with smoothness constraints. The data sets are normalized during inversion after dividing the corresponding norms by No^2, where the number of data points (N) accounts for differences in size and the variance (σ^2) accounts for differences in physical units. The total norm additionally includes the minimization of a model roughness norm as a regularization term that favours models with uniform velocity gradients (Julià *et al.* 2003). The importance of this term is controlled through an *a priori* smoothness parameter, which was determined by trial and error to provide a good visual balance between fitting the observations and stabilizing the velocity–depth profile. Finally, an *a priori* influence factor ($0 < p < 1$) controls the relative importance of each data set to the total RMS misfit. This parameter was set to 0.5 in all inversions, thus giving equal importance to receiver functions and surface wave dispersion.

The initial model for all inversions consisted of a stack of thin layers with fixed thicknesses and uniform velocity that increased with depth. Crustal thickness was 40 km and crustal *S*-velocities increased linearly between 3.5 and 4.0 km s^{-1}. *P*-velocities were obtained by assuming a uniform *Vp*/*Vs* ratio of 1.75 and density was calculated from *P*-velocity using an empirical relationship (Berteussen 1977). In the upper mantle a velocity of 4.5 km s^{-1} was assumed down to 150 km, merging to PREM (Preliminary Reference Earth Model) velocities at 425 km depth. The thicknesses of the layers were 2.5 km down to 60 km depth, 5.0 km down to 150 km depth and 10 km at larger depths. If the station were sitting on sedimentary rocks, then the thickness of the top layer was reduced to 1.5 or 2.0 km to improve the fit to the initial portion of the receiver function waveforms. Although the models were parametrized down to the mantle transition zone, only the top 250 km were inverted for; deeper structure was constrained to keep PREM-like values to account for partial sensitivity of long-period dispersion to deep structure (Julià *et al.* 2003).

In order to better constrain sedimentary structure, stations located within the sedimentary basins (see Fig. 1) also inverted receiver functions obtained at Gaussian widths of 5.0 ($f < 2.4$ Hz). These receiver functions were pre-processed identically to the lower frequency ones, except for the use of smaller time windows (–10 to 60 s) and higher sampling rates (20 sps) to allow for the augmented frequency content. Afterwards the same processing steps were applied as in the previous receiver function calculations.

Results for the broad-band station MASS (Fig. 5), within the Central Tucano sub-basin, display a visually satisfactory match between observations and predictions for both receiver functions and dispersion velocities, with some minor misfits for the waveforms with the highest frequency content. Note that, as this station is located within a sedimentary basin, it includes receiver functions for three different Gaussian widths (1.0, 2.5 and 5.0). There were a total of four receiver function bins formed for this station (recall Fig. 4) and each of the receiver function waveforms was given equal weight within the receiver function data set during inversion. The velocity–depth profile reveals slow *S*-velocities of <3.0 km s^{-1} down to 5 km depth, which likely corresponds to the sedimentary layer. Crustal

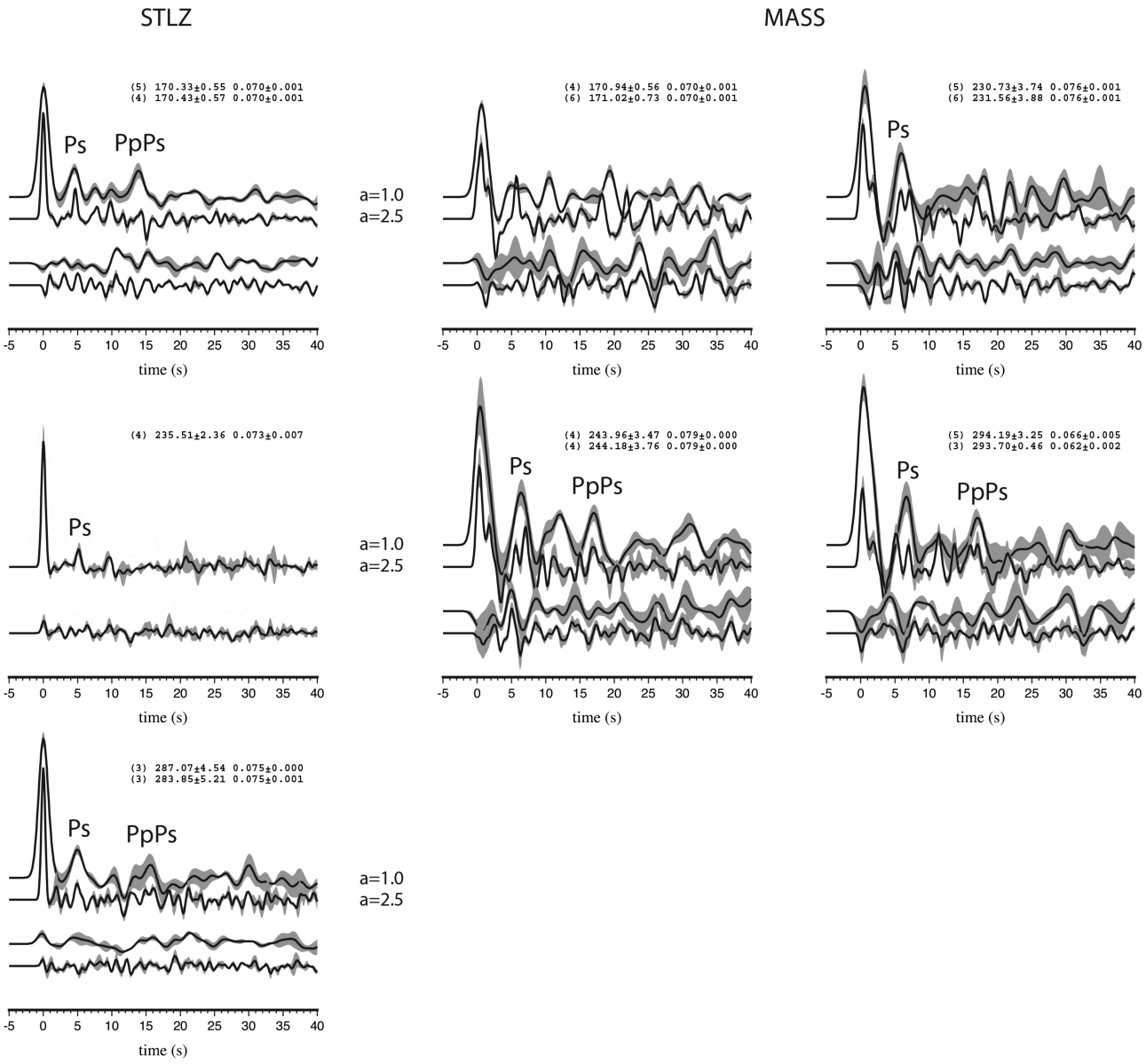

Figure 4. Stacked receiver functions (radial and tranverse) with Gaussian width of 2.5 ($f < 1.2$Hz) for broad-band stations MASS and short-period station STLZ, located in the Tucano basin and the São Francisco Craton, respectively. The average receiver function is shown in black, with 1σ-confidence bounds indicated by the grey shade. Station name, number of stacked receiver functions, backazimuth and ray parameter ranges within each group are indicated on top of each panel.

velocities are under 4.0 km s^{-1} down to 32.5 km depth (except for a small high-velocity layer at 18–20 km depth) and slightly above 4.0 km s^{-1} down to 42.5 km depth, where they gradually increase to mantle-like velocities (≥4.5 km s^{-1}).

Results for the short-period station STLZ, in the São Francisco craton, are shown in Fig. 6. Note that this station did not include receiver functions at high frequencies due to the absence of sedimentary rocks. The observed receiver functions are well matched by the corresponding predictions for all groups, as well as the dispersion velocities. The inverted velocity model displays velocities of 3.5 km s^{-1} in the top 10 km and velocities well under 4.0 km s^{-1} down to 36 km depth, where a small fast-velocity layer (>4.0 km s^{-1}) is observed before reaching mantle-like velocities at about 41 km depth.

The inverted velocity models from all the stations considered in this study are shown in Fig. 7. For the stations within the RTJ rift basins (MSQT, MASS, STAM), along the western flank of the Northern and Central Tucano basin (MACU, STLZ), and within the on-shore Sergipe-Alagoas basin (RCLO) a high velocity (≥4.0 km s^{-1}) lower crust is present. Stations located well within the neighboring São Francisco craton (NBPN, NBCP, PDCB) and Borborema Province (NBTA, RDDO, NBLA, NBAN), on the other hand, show velocity–depth profiles with *S*-velocity under 4.0 km s^{-1} for the entire crustal section. Also note that station NBLA, located immediately East of the Central Tucano sub-basin, displays a very thin crust of just 33.5 km, and that stations NBCP and PDCB, despite being very close to each other, show significant differences in crustal structure.

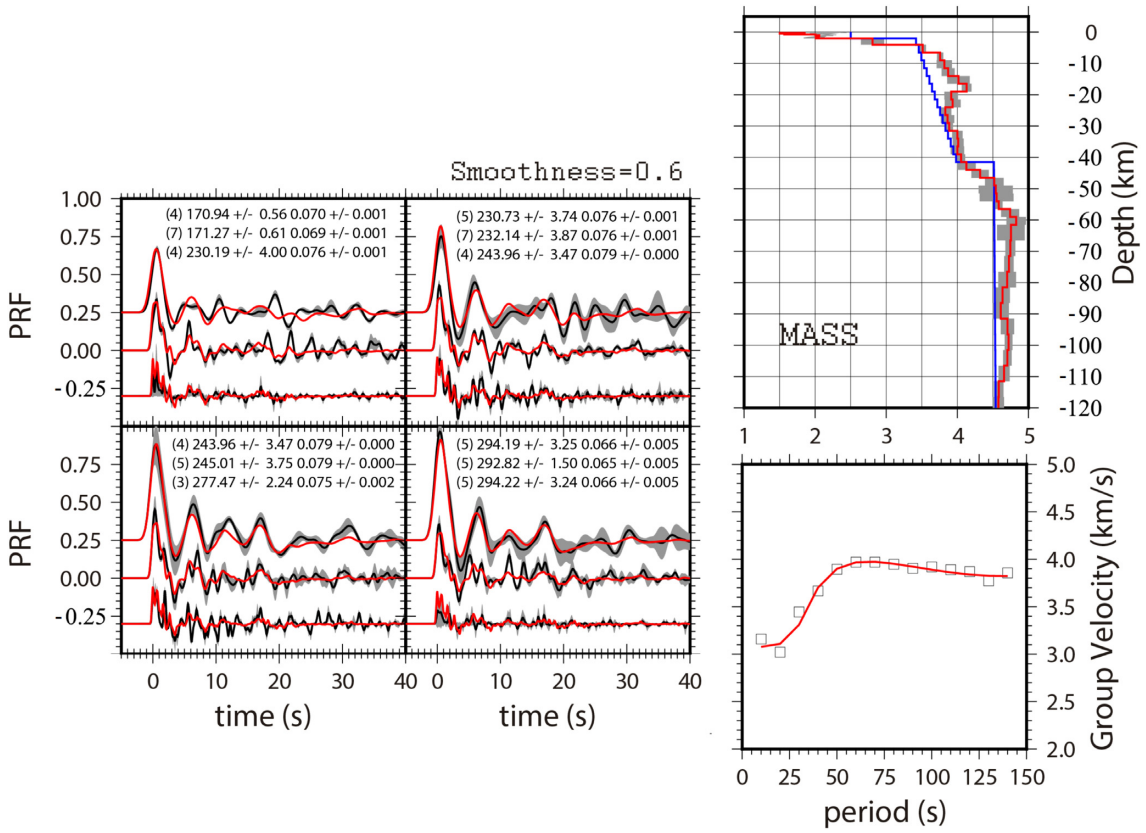

Figure 5. Joint inversion results for station MASS. On the left, four receiver function groups for up to three Gaussian widths are displayed (from top to bottom, $a = 1.0$, $a = 2.5$, $a = 5.0$); predictions are shown as red lines and observations as black lines. In the upper right, the inverted velocity model (*S*-velocity) is displayed; blue line is the initial model, red line is the inverted model and the grey shadow denotes the 2σ-confidence bounds. Confidence bounds were developed after jointly inverting the dispersion curve with each of the receiver function groups independently, and computing the velocity standard deviations from the ensemble of independently inverted models. In the lower right, the dispersion velocities are shown; red line is prediction and the squares observations. The Moho for this station is at around 46 km depth.

4.2 *H–κ* stacking

Independent estimates of crustal thickness (H) and bulk Vp/Vs ratio (κ) can be developed from the same receiver function data set through the H–κ stacking approach of Zhu & Kanamori (2000). In that approach, the stacking of receiver functions is performed along theoretical phase-moveout curves in the H–κ domain and the estimates are obtained from the maximum of the s(H,κ) function defined as

$$S\ (H, \kappa) = \omega_1\, r\,(t_1) + \omega_2 r\,(t_2) - \ \omega_3 r\,(t_3)\,, \qquad (1)$$

where $r(t)$ is the radial receiver function evaluated at t_i, the P_s, $P_P P_S$ and $P_P S_S + P_S P_S$ are S–P times for given pair of crustal thickness and V_P/V_S ratio, and the ω_i are *a priori* weighting factors ($\sum^{\omega_i} = 1$). To compute the S–P times an independent estimate of the P-wave velocity has to be assumed, and a grid-search process is then implemented to find the maximum of the H–κ stacking surface. In this study we assumed a P-wave velocity of 6.5 km s^{-1}, based on the average P-velocity of a nearby refraction study (Soares *et al.* 2011) and consistent with the global average for the continental crust of Christensen & Mooney (1995), and restricted the grid-search within windows of crustal thickness that enclosed the estimates from the corresponding joint inversion models to avoid artefacts from complex structure (Ogden *et al.* 2019). Weights were attributed according to the quality of individual phases, implying that phases with a higher quality are attributed a higher weight (see Table 2). Uncertainties for both H and κ were produced from the model covariance matrix using a bootstrap approach (Efron & Tibshirani 1991), with 200 replications.

Fig. 8 illustrates the performance of this approach at two stations in our study area, one on top of the Tucano basin (MASS) and one located on the São Francisco craton (STLZ). The results for station STLZ are displayed in Fig. 8(a). In most of the receiver functions for this station, the P_S and $P_P P_S$ phases display large amplitudes and thus relatively large weights of 0.5 and 0.5 are given; for the $P_P S_S + P_S P_S$ phase, however, the amplitude is negligible and a zero weight is applied. A crustal thickness of 41.3 ± 0.9 km and a Vp/Vs ratio of 1.70 ± 0.03 were obtained, which corresponds well with the expected thick crust and a more felsic composition for the São Fransisco Craton (Assumpção *et al.* 2004; Luz *et al.* 2015; Nemocon *et al.* 2021). Fig. 8(b) shows the results for station MASS. At this station the P_S phase is most clear, so a large weight of 0.6 is given; the $P_P P_S$ phase, on the other hand, is not present in some waveforms and a value of just 0.3 is chosen; for the $P_P S_S + P_S P_S$ phase, the smallest weight of 0.1 was applied since it appears in just a few waveforms. A crustal thickness of 41.9 ± 1.2 km and and a Vp/Vs ratio of 1.81 ± 0.04 were obtained for this station, which reveals an unexpected thick crust for this sedimentary basin.

The H–κ stacking results for all available stations are summarized in Table 2, along with a comparison to the crustal thickness estimates from the joint inversion (Fig. 7). Uncertainties are reported

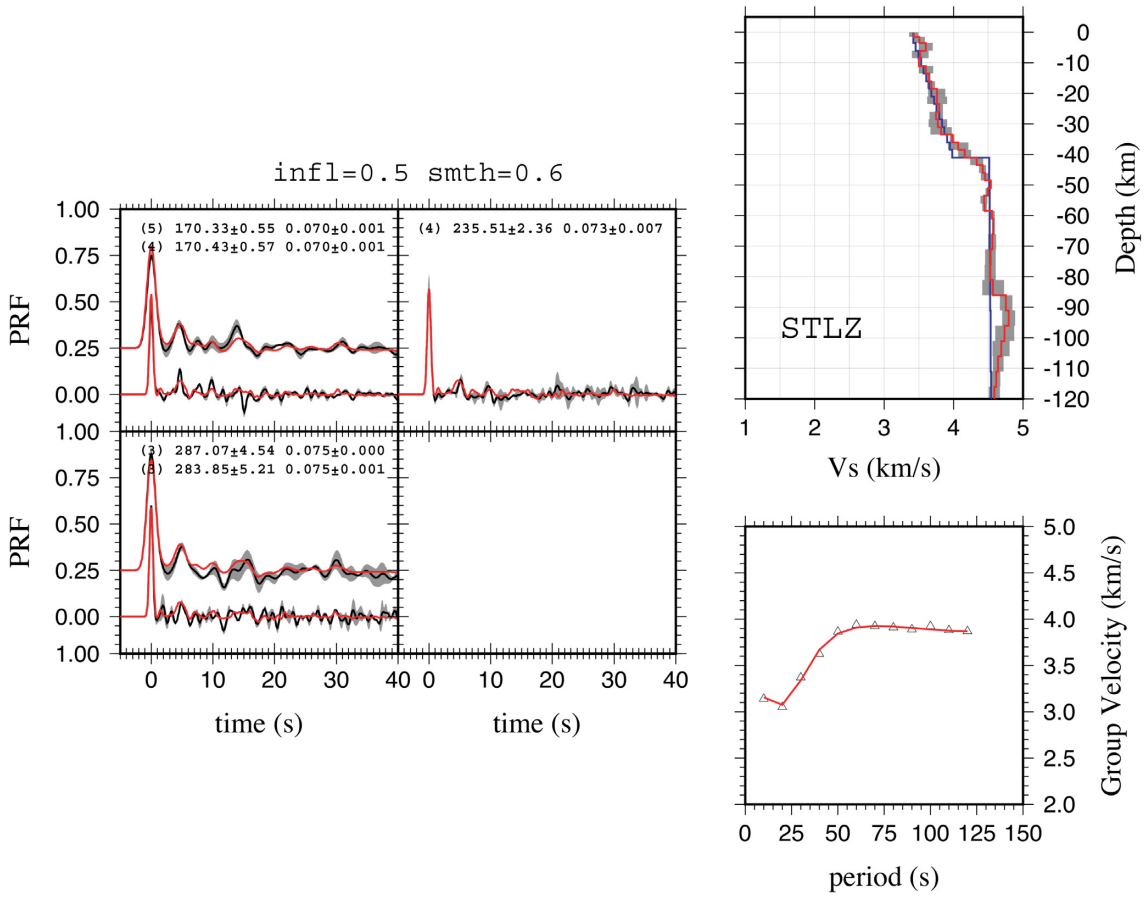

Figure 6. Same caption as in Fig. 5, for station STLZ. Moho thickness for this station is around 41 km.

as 2σ-confidence bounds, while the covariance between H and κ is reported as a normalized percentage. The covariance is expected to be large and negative due to the larger phase moveout of the multiply reverberated phases (Julià & Mejía 2004). Only station RDDO displays a covariance below 70 per cent, which suggests results at this station are less reliable. Note that stations that did not produce more than 3 receiver functions were not included, since it was not possible to obtain reliable estimates.

A comparison of crustal thickness estimates from the H–κ stacking and joint inversion approaches (Fig. 9) reveals that, in general, the H–κ stacking approach is capable of finding crustal thickness estimates that are consistent with those inferred from the velocity–depth profiles. The main discrepancies are for stations MSQT, MACU and RCLO, where crustal H–κ thicknesses of 33–36 km contrast with values of 40.0 km or more estimated from the joint inversion. A close inspection of the corresponding velocity–depth profiles (Fig. 7) reveals that the H–κ thickness estimates do not correspond to the base of the crust but the top of a fast-velocity lowermost crust. Thus, H–κ thicknesses and Vp/Vs ratios for those stations reflect averages for the upper and middle crusts, rather than averages for the entire crustal column. It is interesting to note that a similar effect was reported in Ogden *et al.* (2019) for stations located on top of the Ethiopian Traps of East Africa.

For the stations sampling the entire crustal column, the H–κ stacking estimates reveal the São Francisco craton has an average crustal thicknesses of 41.6 ± 1.1 km and relatively low Vp/Vs values averaging 1.71 ± 0.02, while stations on the Borborema Province have crustal thicknesses of 35.6 ± 1.0 km and Vp/Vs ratios averaging 1.72 ± 0.04. They also confirm an anomalously thin crust under station NBLA. These results are found consistent with those reported in the independent receiver function studies of Luz *et al.* (2015) and Nemocon *et al.* (2021) and the seismic refraction line of Lopes (2017). Stations sampling only the shallower crustal portions are located within the outlines of the sedimentary basins or close to them. Two of those stations (MACU, RCLO) reveal Vp/Vs ratios well below 1.70, as expected for shallower crustal lithologies (Christensen 1996), while one of them (MSQT) displays a larger Vp/Vs ratio of 1.79 (although confidence bounds are sizeable). Large Vp/Vs ratios are likely due to the presence of a locally thicker sedimentary cover.

5 DISCUSSION

As mentioned earlier, several models have been proposed to explain the formation and evolution of the RTJ rift and associated marginal basins (Blaich *et al.* 2008; Magnavita *et al.* 1994; Milani & Davison 1988; Mohriak *et al.* 2000; Ussami *et al.* 1986). These models mostly revolve around pure shear or simple shear being the main mode of extension in the lithosphere, and mapping crustal thickness has been the main tool for supporting new models and rejecting old ones. Interestingly, crustal thickness had been mapped quasi-exclusively through gravity modelling with results that conflicted with one another: while one set of modelling results saw crustal thinning was offset with respect to basin depocentres (Castro Jr 1987;

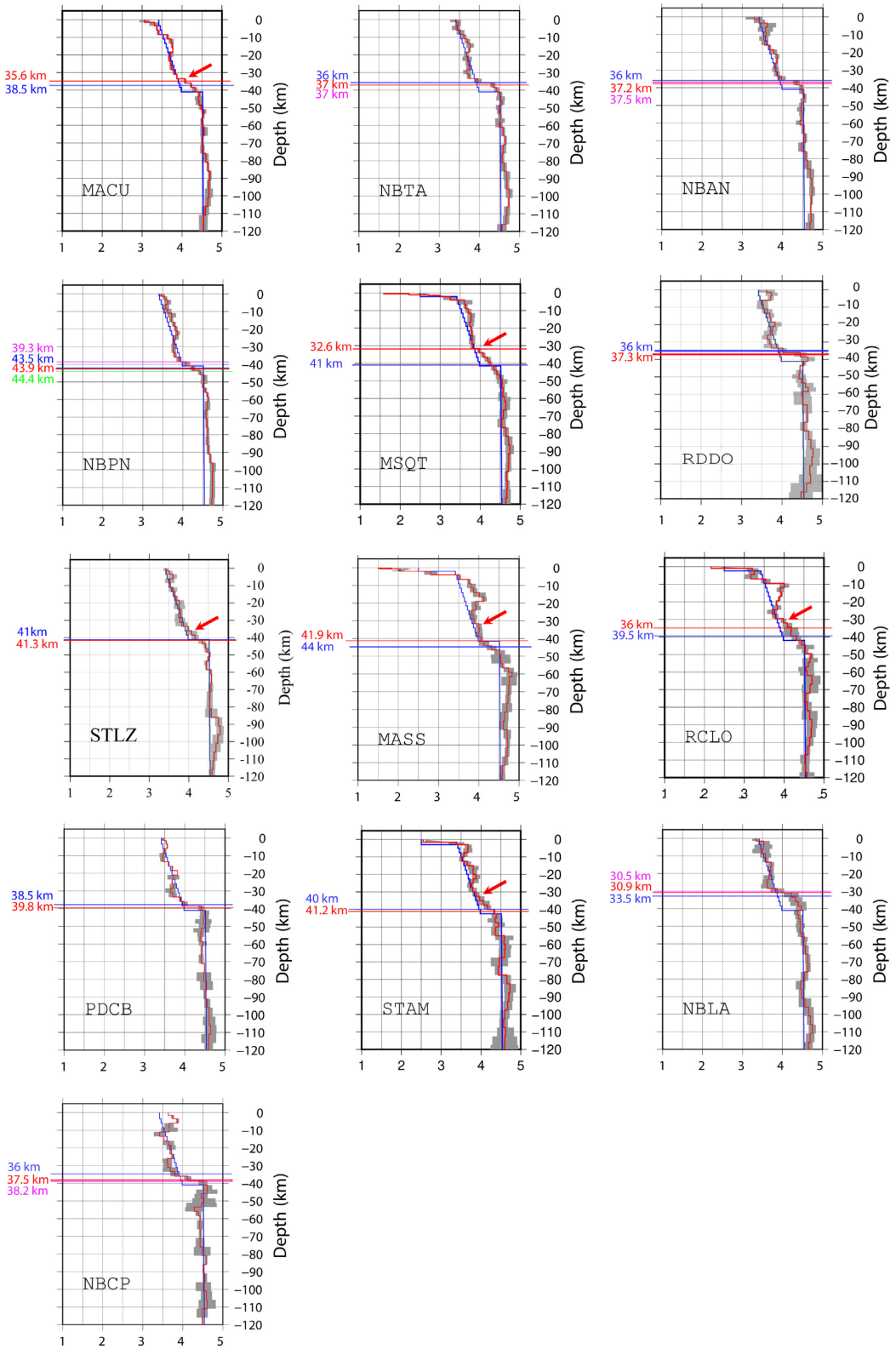

Figure 7. Joint inversion models for all the stations considered in this study. Red and blue profiles represent the inverted and starting models, respectively. Crustal depths were estimated as the top of the first layer that exceeded 4.3 km s^{-1} and are indicated as horizontal red lines. Crustal depths from H–κ stacking are indicated as blue horizontal lines, along with independent estimates from Nemocon *et al*. (2021) (green) and Luz *et al.* (2015) (magenta), for comparison. A high-velocity lower crust is indicated through a small red arrow pointing to the first layer exceeding 4.0 km s^{-1}, when observed. Grey shadows represent confidence bounds for each inverted model.

Table 2. Crustal thickness estimates from H–κ stacking and joint inversion for a Gaussian width of 2.5.

Station name	H (km)	H (km) joint	κ	Vp (km s^{-1})	Weights	Covariance (per cent)
			Stations inside sedimentary basins			
ESPL	35.4 ± 0.7	–	1.72 ± 0.11	6.5	0.6/0.3/0.1	-78.9
MASS	41.9 ± 1.2	44.0 ± 2.5	1.81 ± 0.04	6.5	0.6/0.3/0.1	-74.4
MSQT∗	32.6 ± 1.4	41.5 ± 2.5	1.79 ± 0.04	6.5	0.6/0.3/0.1	-97.3
RCLO∗	36.0 ± 1.8	42.5 ± 2.5	1.63 ± 0.07	6.5	0.6/0.3/0.1	-83.6
STAM	41.2 ± 1.0	39.5 ± 2.5	1.73 ± 0.03	6.5	0.6/0.3/0.1	-93.4
			Stations outside of sedimentary basins			
MACU∗	35.6 ± 0.9	40.0 ± 2.5	1.65 ± 0.03	6.5	0.6/0.3/0.1	-86.3
NBAN	37.2 ± 0.6	36.0 ± 2.5	1.72 ± 0.02	6.5	0.5/0.3/0.2	-83.6
NBCP	37.5 ± 2.0	36.0 ± 2.5	1.78 ± 0.05	6.5	0.5/0.3/0.2	-98.2
NBLA	30.9 ± 1.5	33.5 ± 2.5	1.75 ± 0.04	6.5	0.5/0.3/0.2	-97.1
NBPE	44.6 ± 1.2	–	1.70 ± 0.03	6.5	0.5/0.3/0.2	-86.9
NBPN	43.9 ± 1.0	43.5 ± 2.5	1.68 ± 0.02	6.5	0.5/0.3/0.2	-81.2
NBTA	37.0 ± 0.1	36.0 ± 2.5	1.72 ± 0.00	6.5	0.5/0.3/0.2	-80.0
PDCB	39.8 ± 0.9	38.5 ± 2.5	1.72 ± 0.02	6.5	0.5/0.4/0.1	-92.6
RDDO	37.3 ± 0.4	36.0 ± 2.5	1.68 ± 0.01	6.5	0.5/0.3/0.2	-56.8
STLZ	41.3 ± 0.9	41.0 ± 2.5	1.70 ± 0.03	6.5	0.5/0.5/0.0	-72.7
UAUA	42.7 ± 0.4	–	1.71 ± 0.01	6.5	0.5/0.3/0.2	-94.7

∗Stations where crustal thickness estimates do not match.

Mohriak *et al.* 2000; Ussami *et al.* 1986), another set saw crustal thinning right underneath (Blaich *et al.* 2008; Milani & Davison 1988). The use of different data sets and different processing techniques might explain, at least in part, some of the differences. Milani & Davison (1988), for instance, argued that Ussami *et al.* (1986) used a simplified Bouguer anomaly map lacking flanking anomalies up to 50 mGal observed in more detailed maps, resulting in crustal models with no thinning under the rift. And Mohriak *et al.* (2000) determined crustal transects that were more consistent with those of Ussami *et al.* (1986), even after adding data from a proprietary reconnaissance gravity survey acquired by Petrobras that was not available in previous studies and extensive constraints from seismic reflection profiling. Nonetheless, differences might have also arisen from the non-uniqueness in gravity modelling (e.g. Blakely 1996), which is often mitigated through the use of *a priori* information on the sought-after solution. Indeed, gravity modelled transects from Blaich *et al.* (2008) included a thick high-density lower crust under the off-shore Sergipe-Alagoas and Jacuipe sub-basins that was missing in other studies, only to seek consistency with independent seismic profiles.

Our results on crustal thickness yield values of 41.8 ± 2.5 km for the São Francisco craton, 36.2 ± 2.5 km for the Borborema Province and 41.6 ± 2.5 for the RTJ rift. These values are considerably thicker than those determined from any of the gravity modelled transects mentioned above, probably because of oversimplification of crustal structure as a single layer of uniform density and non-uniqueness. Taken at face value, our results would suggest a general lack of crustal stretching during the formation of the RTJ basins and support models that invoke simple shear (Castro Jr 1987; Ussami *et al.* 1986). The required detachment surface could easily match the surface half-graben architecture through either a listric prolongation of the master fault (Castro Jr 1987) or a straight prolongation of the shallow-dipping basement surface (Ussami *et al.* 1986) down to lithospheric depths (recall Fig. 3). Moreover, as the only instance of thin crust in our study has been found along the eastern flank of the Central Tucano basin (Fig. 9), we might be tempted to favour eastward dipping for the postulated detachment surface (Ussami *et al.* 1986).

Interestingly, our velocity–depth profiles show that the lack of crustal thinning under the RTJ rift is due to a relatively thick layer of fast-velocity material in the lowermost crust (Fig. 10). Such a fast-velocity layer is also observed under two stations flanking the Tucano basin to the West, but it is generally not observed under the stations within the São Francisco craton and the Borborema Province, suggesting it was not part of the original crust prior to rifting. Serpentinized peridotite is a commonly invoked interpretation for a fast-velocity lower crust in continental rifted margins, requiring large detachments crossing the entire crustal section—such as those proposed by Ussami *et al.* (1986) and Castro Jr (1987)—so that water can permeate and reach lower crustal levels (e.g. Rüpke *et al.* 2013). However, considering the thick continental crust under the RTJ basins and the non-marine character of their syn-rift deposition, we find this possibility quite unlikely. A more plausible mechanism for producing such a fast lowermost crust would be magmatic intrusion or underplating of Precambrian basement crust. Recall that magmatic intrusions were considered by Mohriak *et al.* (2000) and Magnavita *et al.* (1994) in spite of the Tucano rift being almost devoid of any volcanic rocks.

If our interpretation were correct, then our results would fit quite well with the flexural cantilever model of Magnativa *et al.* (1994). Recall that the flexural cantilever model is a coupled simple-shear/pure-shear model in which extension along planar faults in the upper crust is balanced with pure-shear deformation in the lower crust and lithospheric mantle. Magnavita *et al.* (1994) argued that associated rift-flank uplift and erosion of the footwall could explain the Aptian unconformity identified in the sedimentary record. Moreover, through numerical modelling, Magnavita *et al.* (1994) showed that rift-flank uplift and erosion could result in as much as 5 km of crust being removed, which would explain the anomalously thin crust identified under station NBLA in our study. Considering an average 36-km-thick crust prior to basin formation (Luz *et al.* 2015), that amount of erosion would match the 33.5 km observed under this station quite nicely. Magnavita *et al.* (1994) also invoked mafic underplating to support regional uplift of the basin and subsequent erosion of the post-rift sediments, which matches well with

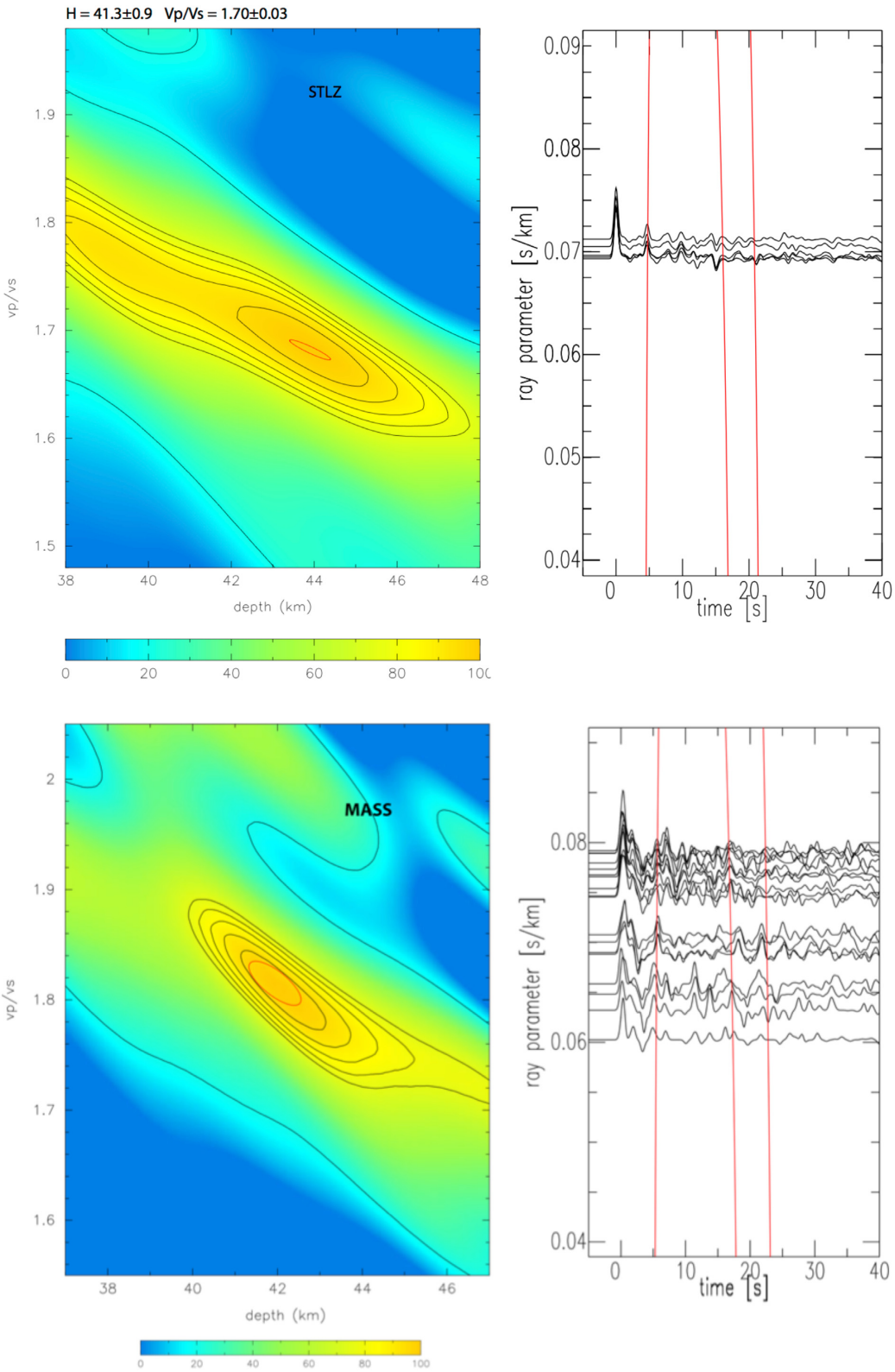

Figure 8. Estimates of crustal thickness (H) and Vp/Vs ratio (κ) from the H–κ stacking approach at stations STLZ (upper left) and MASS (lower left) and their respective receiver functions (upper and lower right). The red ellipse represents the 1σ-confidence contour from the bootstrap analysis. The red lines on the right panels represent the S–P times (phase-moveout curve) corresponding to the maximum of the H–κ stacking surface.

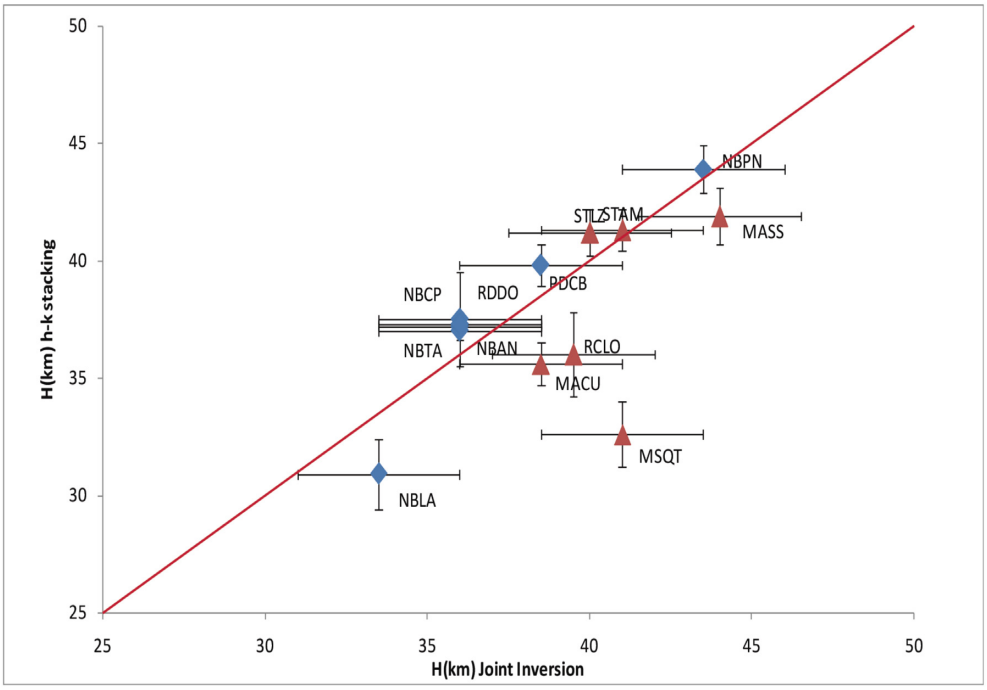

Figure 9. Comparison of crustal thickness estimates from the *H–κ* stacking (*y*-axis) from the joint inversion (*x*-axis) approaches. Stations with and without a high-velocity lower crust are noted as red and blue diamonds, respectively. Note the overall consistency, within confidence bounds, from both approaches.

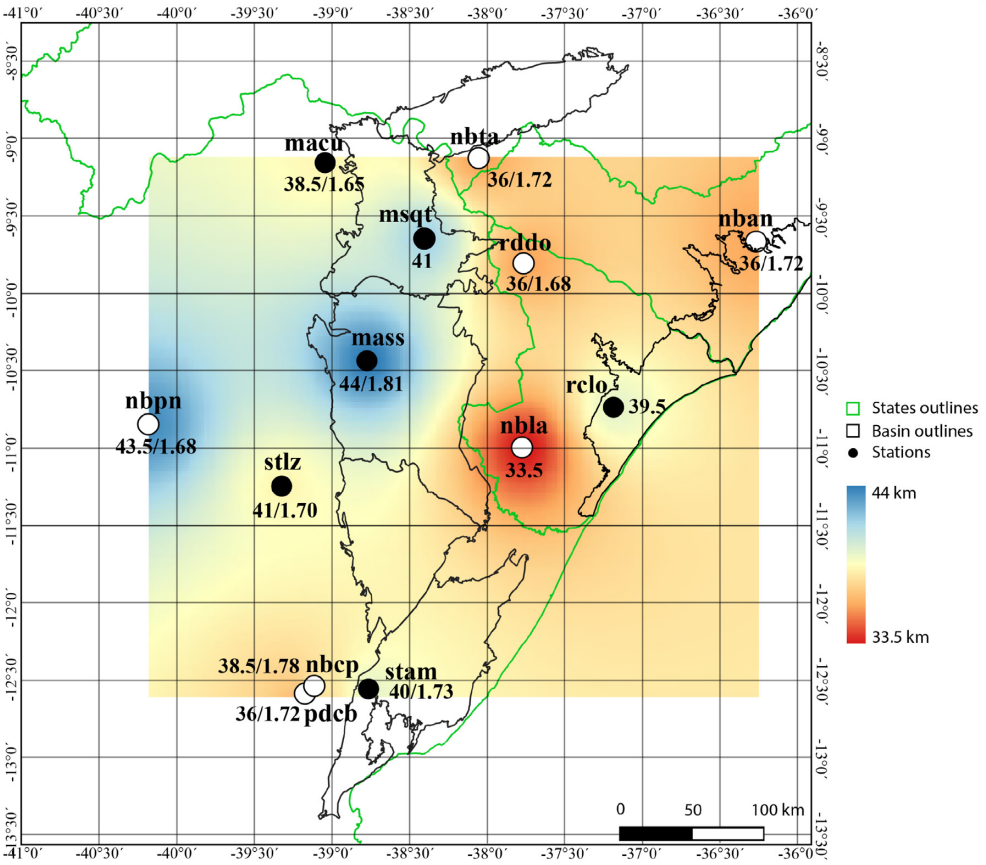

Figure 10. Estimates of crustal thickness (joint inversion) and *Vp*/*Vs* ratio for all the stations that yielded results in the Recôncavo–Tucano-Jatobá rift and surrounding areas. Stations without *Vp*/*Vs* ratio are those for which *H–κ* crustal thickness did not match that inferred from the joint inversion models. Stations West of the basins are on top of the São Francisco Cráton and stations East of the basins are on top of the Borborema Province. Stations have been colour coded according to the presence (black) or absence (white) of a fast-velocity lowermost crust. Basin outlines are shown as a solid black line.

our interpretation of the fast-velocity layer under the RTJ rift basin stations resulting from magmatic intrusions. The presence of such a layer beneath two stations along the western flank of the Tucano basin (MACU, STLZ) is more puzzling, but could also be explained through regional uplift and erosion. Assuming that the Tucano basin had been larger than suggested by its actual limits and included the crust under those stations, uplift and erosion could have removed any sedimentary sequences deposited prior to the underplating event and leave an outcropping basement crust with a fast-velocity mafic layer at its bottom.

It is nonetheless worth noting that, although the flexural cantilever model predicts a rise of the lithosphere/asthenosphere boundary and an increase of the geothermal gradient during extension, it does not take into account any syn-rift magmatism from eventual decompression and melting of the mantle (White & McKenzie 1989). Recall that syn-rift magmatism was contemplated by Mohriak *et al.* (2000), as they observed thick wedges of seaward dipping reflectors on seismic profiles crossing the Sergipe-Alagoas basin. Also, recent investigations of this basin by onshore-offshore seismic refraction have found anomalously fast lower continental crust *P*-velocity in the necking zone (Pinheiro *et al.* 2018), which gives further support to the occurrence of syn-rift magmatism. Another hypothesis for the fast-velocity layer under the RTJ rift basins could therefore be that syn-rift magmatic intrusions were responsible for its formation. Note that this would not necessarily exclude the episode of post-rift magmatism postulated by Magnavita *et al.* (1994). Assuming Airy isostasy and an average crustal density for the magmas, those authors noted that approximately 3.5 km of underplated material would be necessary to explain the 600 m of uplift required to erase the post-rift sequences from the sedimentary record. That value is smaller than the observed 5–8 km thickness for the fast-velocity layer under our RTJ rift stations, suggesting that the observed layer could be the combined effect of both syn- and post-rift magmatism. At a number of locations around the globe, lower crustal magmatic intrusions have been inferred as the main driver of syn-rift basin subsidence, with notable examples being the Parnaíba cratonic basin (Tozer *et al.* 2017) and the Mozambican Coastal Plain (Moulin *et al.* 2020). In the RTJ basin, a regional event may have worked against subsidence shortly after emplacement of intrusions in the lower crust as attested by the widespread extent of the Aptian unconformity covering the entire central segment of the South Atlantic (Chaboureau *et al.* 2013).

Regardless of a syn-rift or post-rift nature for the magmatic lower crust, or a mixture of both, stretching and thinning of the Precambrian basement crust prior to rift formation seems to be required to preserve crustal thickness after magmatic addition. In the syn-rift case, it would also be critical to trigger decompression melting under the basin. Thus, returning to the original debate of how extension was accommodated during rifting, we conclude that pure-shear deformation of the lower crust and lithospheric mantle had to take place under the RTJ rift basins.

6 CONCLUSIONS

The crustal structure in and around the RTJ rift has been determined from the joint inversion of receiver functions and surface-wave dispersion velocities. Our results have revealed that the crust is about 41.6 ± 2.5 km thick under the basin, similar to thicknesses in the outcropping São Francisco craton along the western flank (41.8 ± 2.5 km) and a bit larger than thicknesses in the outcropping Borborema Province along the eastern flank (36.2 ± 2.5 km). The crustal structure under the RTJ rift basins displays a layer of fast velocity ($Vs > 4.0$ km s^{-1}) material in the lowermost crust that has been interpreted as resulting from magmatic intrusion of extended crust under the rift, supporting models that invoke pure shear extension of the lower crust and lithospheric mantle. It has also been identified as a source of buoyancy along the rift, consistent with the removal of post-rift sedimentation through regional uplift and erosion proposed in the flexural cantilever model of Magnavita *et al.* (1994). We have also observed an instance of unexpectedly thin crust (33.5 ± 2.5 km) in the eastern flank of the Central Tucano basin, next to the main rift fault. This observation has been found consistent with simple shear extension in the upper crust causing footwall uplift and rift flank erosion, again consistent with the flexural cantilever model of Magnavita *et al.* (1994). We have also proposed that the Tucano basin might have extended beyond its present limits before the underplating event, thus explaining the presence of fast-velocity material along its western flank.

ACKNOWLEDGMENTS

Financial support for this study was provided by Petróleo Brasileiro S.A. (Petrobras, grant number 5850.0106463.17.9) to acquire the seismic data set and the Coordenação de Aperfeiçoamento de Pessoal de Nível Superior–Comité Français d'Evaluation de la Cóoperation Universitaire avec le Brésil (CAPES-COFECUB, grant number 88881.192828/2018-01) for networking. The authors also acknowledge Petrobras for granting a 2-yr scholarship to complete an MSc degree at the Universidade Federal do Rio Grande do Norte (MFD), and for a generous research fellowship (JJ) during the realization of this study.

DATA AVAILABILITY

Software for receiver function analysis is freely available upon request to the corresponding author. Data from the *Rede Sismográfica Brasileira* (RSBR) can be downloaded from http://rsbr.gov.br; all other data are proprietary.

REFERENCES

Ammon, C. J., Randall, G. E. & Zandt, G., 1990. On the nonuniqueness of receiver function inversions, *J. geophys. Res.,* **95**(B10), 15 303–15 318.

Assumpção, M., An, M., Bianchi, M., França, G. S. L., Rocha, M., Barbosa, J. R. & Berrocal, J., 2004. Seismic studies of the Brasília fold belt at the western border of the São Francisco Craton, Central Brazil, using receiver function, surface-wave dispersion and teleseismic tomography, *Tectonophysics,* **388**(1–4), 173–185.

Berteussen, K. A., 1977. Moho depth determinations based on spectral-ratio analysis of NORSAR long-period P waves, *Phys. Earth planet. Inter.,* **15**(1), 13–27.

Bianchi, M.B. *et al.*, 2018. The Brazilian Seismographic Network (RSBR): Improving Seismic Monitoring in Brazil, *Seismological Research Letters,* **89**(2A), 452–457.

Blaich, O. A., Tsikalas, F. & Faleide, J. I., 2008. Northeastern Brazilian margin: regional tectonic evolution based on integrated analysis of seismic reflection and potential field data and modelling, *Tectonophysics,* **458**(1–4), 51–67.

Blakely, R. J., 1996. *Potential Theory in Gravity and Magnetic Applications*. Cambridge Univ. Press.

Caixeta, J. M., Bueno, G. V., Magnavita, L. P. & Feijó, L. P., 1994. Bacias do Recôncavo, Tucano e Jatobá, *Boletim de Geociências Da Petrobrás,* **8**(1), 163–172.

Castro, A. C. M., Jr., 1987. The northeastern Brazil and Gabon basins: a double rifting system associated with multiple crustal detachment surfaces, *Tectonics,* **6**(6), 727–738.

Cedraz, V., Julià, J. & Assumpção, M., 2020. Joint inversion of receiver functions and surface-wave dispersion in the Pantanal Wetlands: implications for basin formation, *J. geophys. Res.,* **125**(2), e2019JB018337, doi:10.1029/2019JB018337.

Chaboureau, A.-C., Guillocheau, F., Robin, C., Rohais, S., Moulin, M. & Aslanian, D., 2013. Paleogeographic evolution of the central segment of the South Atlantic during Early Cretaceous times: paleotopographic and geodynamic implications, *Tectonophysics,* **604,** 191–223.

Chang, H. K., Kowsman, R. O. & Figueiredo, A. M. F., 1988. New concepts on the development of east Brazilian marginal basins, *Int. Un. Geol. Sci.,* **11**(3), 194–202.

Christensen, N. I. & Mooney, W. D., 1995. Seismic velocity structure and composition of the continental crust: a global view, *J. geophys. Res.,* **100**(B6), 9761–9788.

Christensen, N.J. 1996. Poisson's ratio and crustal seismology, *J. Geophys Res.,* **101,** 3139–3156.

Cloetingh, S. & Burov, E., 2011. Lithospheric folding and sedimentary basin evolution: a review and analysis of formation mechanisms, *Basin Res.,* **23**(3), 257–290.

Coelho, D.L.O., Julià, J., Rodríguez-Tribaldos, V. & White, N., 2018. Deep crustal structure of the Parnaíba basin of NE Brazil from receiver function analysis: implications for basin subsidence, in *Cratonic Basin Formation: A Case Study of the Parnaíba Basin of Brazil,* Vol. **472,** eds DalY, M. C., Fuck, R. A., Julià, J., Macdonald, D. I. M. & Watts, A. B., Geological Society, London, Special Publications, doi:10.1144/SP472.8.

Davison, I., Batista Guimarães Teixeira, J., Da Glória Da Silva, M., Barretto Da Rocha Neto, M. & Martins Vieira Matos, F., 1988. The Rio Itapicuru greenstone belt, Bahia, Brazil: structure and stratigraphical outline, *Precambrian Res.,* **42**(1–2), 1–17.

Dziewonski, A., Bloch, S. & Landisman, M., 1969. A technique for the analysis of transient seismic signals, *Bull. seism. Soc. Am.,* **59**(1), 427–444.

Efron, B. & Tibshirani, R., 1991. Statistical data analysis in the computer age, *Science,* **253**(5018), 390–395.

Feng, M., Assumpção, M. & Van der Lee, S., 2004. Group-velocity tomography and lithospheric S-velocity structure of the South American continent, *Phys. Earth planet. Inter.,* **147**(4), 315–331.

Herrin, E. & Goforth, T., 1977. Phase-matched filters: application to the study of Rayleigh waves, *Bull. seism. Soc. Am.,* **67**(5), 1259–1275.

Julià, J., 2007. Constraining velocity and density contrasts across the crust–mantle boundary with receiver function amplitudes, *Geophys. J. Int.,* **171,** 286–301.

Julià, J., Ammon, C. J. & Herrmann, R. B., 2003. Lithospheric structure of the Arabian Shield from the joint inversion of receiver functions and surface-wave group velocities, *Tectonophysics,* **371**(1–4), 1–21.

Julia, J., Ammon, C. J., Herrmann, R. B. & Correig, A. M., 2000. Joint inversion of receiver function and surface wave dispersion observations, *Geophys. J. Int.,* **143**(1), 99–112.

Julia`, J., Herrmann, R. B., Ammon, C. J. & Akinci, A., 2004. Evaluation of deep sediment velocity structure in the New Madrid Seismic Zone, *Bull. seism. Soc. Am.,* **94**(1), 334–340.

Julià, J. & Mejía, J., 2004. Thickness and Vp/Vs ratio of the Iberian crust, *Geophys. J. Int.,* **156,** 59–72.

Julià, J., Vila, J. & Macià, R., 1998. The receiver structure beneath the Ebro basin, Iberian Peninsula, *Bull. Seism. Soc. Am.,* **88**(6), 1538–1547.

Kusznir, N. J. & Ziegler, P. A., 1992. The mechanics of continental extension and sedimentary basin formation: a simple-shear/pure-shear flexural cantilever model, *Tectonophysics,* **215**(1–2), 117–131.

Langston, C. A., 1979. Structure under Mount Rainier, Washington, inferred from teleseismic body waves, *J. geophys. Res.,* **84**(B9), 4749–4762.

Langston, Charles A & Hammer, J. K., 2001. The vertical component P-wave receiver function, *Bull. seism. Soc. Am.,* **91**(6), 1805–1819.

Ligorría, J. P. & Ammon, C. J., 1999. Iterative deconvolution and receiver-function estimation, *Bull. seism. Soc. Am.,* **89**(5), 1395–1400.

Lopes, L.R., 2017. *Modelagem da estrutura crustal sob a porção sul do perfile N-S da Província Borborema e Cráton São Francisco: um estudo de refração sísmica profunda, Bachelor Thesis,* Caçapava do Sul, RS, Universidade Federal do Pampa.

Luz, R. M. N., Julià, J., Nascimento, Do & A., F., 2015. Crustal structure of the eastern Borborema Province, NE Brazil, from the joint inversion of receiver functions and surface wave dispersion: implications for plateau uplift, *J. geophys. Res.,* **120**(5), 3848–3869.

Magnavita, L. P., Davison, I. & Kusznir, N. J., 1994. Rifting, erosion, and uplift history of the Recôncavo-Tucano-Jatobá Rift, northeast Brazil, *Tectonics,* **13**(2), 367–388.

Matos, R. M. D., 1992. The Northeast Brazilian Rift System, *Tectonics,* **11**(4), 766–791.

Matos, R. M. D., 1999. History of the northeast Brazilian rift system: kinematic implications for the break-up between Brazil and West Africa, *Geol. Soc. Spec. Publ.,* **153,** 55–73.

McKenzie, D., 1978. Some remarks on the development of sedimentary basins, *Earth planet. Sci. Lett.,* **40**(1), 25–32.

Milani, E. J. & Davison, I., 1988. Basement control and transfer tectonics in the Recôncavo-Tucano-Jatobá rift, Northeast Brazil, *Tectonophysics,* **154,** 41–70.

Mohriak, W. U., Bassetto, M. & Vieira, I. S., 2000. Tectonic evolution of the rift basins in the northeastern Brazilian region, *Geophys. Monogr. Ser.,* **115,** 293–315.

Moulin, M. *et al.*, 2020. Gondwana breakup: messages from the North Natal Valley, *Terra Nova,* **32,** 205–214.

Nemocon, A.M., Julià, J. & Garcia, X., 2021. Lithospheric structure of the western Borborema Province from receiver functions and surface-wave dispersion: implications for basin inversion, *Tectonophysics,* **816,** 229024, doi:10.1016/j.tecto.2021.229024.

Ogden, C.S., Bastow, I.D., Gilligan, A. & Rondenay, S., 2019. A reappraisal of the H-κ stacking technique: implications for global crustal structure, *Geophys. J. Int.,* **219,** 1491–1513..

Owens, T. J. & Taylor, S. R., 1984. A detailed analysis of broadband P waveforms, *J. geophys. Res.,* **89**(B9), 7783–7795.

Paige, C. C. & Saunders, M. A., 1982. Algorithm 583: LSQR: sparse linear equations and least squares problems, *ACM Trans. Math. Softw. (TOMS),* **8**(2), 195–209.

Pinheiro, J. M. *et al.*, 2018. Lithospheric structuration onshore-offshore of the Sergipe-Alagoas passive margin, NE Brazil, based on wide-angle seismic data, *J. South Am. Earth Sci.,* **88**(October), 649–672.

Rondenay, S., Spieker, K., Sawade, L., Halpaap, F. & Faresveit, M., 2017. GLImER: a new global database of teleseismic receiver functions for imaging Earth structure, *Seismol. Res. Lett.,* **88,** 39–48.

Rüpke, L.H., Schmid, D.W., Pérez-Gussinyé, M. & Hartz, E., 2013. Interrelation between rifting, faulting, sedimentation, and mantle serpentinization during continental margin formation - including examples from the Norwegian Sea, *Geochem. Geophys. Geosyst.,* **14,** 4351–4369.

Silva, H. T. F. da., 1993. *Flooding Surfaces, Depositional Elements, and Accumulation Rates: Characteristics of the Lower Cretaceous Tectonosequence in the Recôncavo Basin, Northeast Brazil*. University of Texas–Austin.

Soares, J.E.P., de Lima, M.V., Fuck, R.A. & de Oliveira, M.P., 2011. Descontinuidade de Moho e velocidade média da crosta sob a linha de rafração sísmica profunda N-S da Província Borborema: uma aproximação por reflexões de alto ângulo. In: Twelfth International Congress of the Brazilian Geophysical Society, *Rio de Janeiro, Annals,* pp.1–4.

Teisserenc, P. & Villemin, J., 1989. Sedimentary basin of Gabon–geology and oil systems.

Tozer, B., Watts, A. B. & Daly, M. C., 2017. Crustal structure, gravity anomalies, and subsidence history of the Parnaíba cratonic basin, Northeast Brazil: structure Parnaíba Cratonic Basin, *J. geophys. Res.,* **122**(7), 5591–5621.

Ussami, N., Karner, G. D. & Bott, M. H. P., 1986. Crustal detachment during South Atlantic rifting and formation of Tucano - Gabon basin system, *Nature,* **322**(6080), 629–632.

Viana, C.F., Gama Junior, E.G., Simões, I.A., Moura, J.A., Fonseca, J.R. & Alves, R.J., 1971. Revisão estratigráfica da Bacia Recôncavo/Tucano, *Boletim Técnico da Petrobras 14,* 157–192.

Wernicke, B., 1985. Uniform-sense normal simple shear of the continental lithosphere, *Can. J. Earth Sci.,* **22**(1), 108–125.

White, R. & McKenzie, D., 1989. Magmatism at rift zones: the generation of volcanic continental margins and flood basalts, *J. geophys. Res.,* **94**(B6), 7685.

Zelt, B. C. & Ellis, R. M., 1999. Receiver-function studies in the Trans-Hudson Orogen, Saskatchewan, *Can. J. Earth Sci.,* **36**(4), 585–603.

Zhu, L. & Kanamori, H., 2000. Moho depth variation in southern California from teleseismic receiver functions, *J. geophys. Res.,* **105,** 2969–2980.

SUPPORTING INFORMATION

Supplementary data are available at *GJI* online.

Supplementarymaterials.pdf

Please note: Oxford University Press is not responsible for the content or functionality of any supporting materials supplied by the authors. Any queries (other than missing material) should be directed to the corresponding author for the paper.